

HOCO formation in astrochemical environments by radical-induced H-abstraction from formic acid

Max N. Markmeyer,¹ Thanja Lamberts^{1,2}*, Jan Meisner,¹† and Johannes Kästner¹★

¹*Institute for Theoretical Chemistry, University of Stuttgart, Pfaffenwaldring 55, D-70569 Stuttgart, Germany*

²*Current address: Leiden Institute of Chemistry, Gorlaeus Laboratories, Leiden University, PO Box 9502, NL-2300 RA Leiden, the Netherlands*

Accepted 2018 September 21. Received 2018 September 5; in original form 2018 August 3

ABSTRACT

Rate constants for the radical-induced hydrogen abstraction from formic acid, HCOOH, are presented here. Only those reactions leading to the formation of HOCO were investigated. The astrochemically relevant radicals OH, NH₂, and H were considered to induce the H-abstraction. Tunnelling was taken into account by using the instanton method for rate constant calculations. For reactions relevant on grain surfaces, the unimolecular rate constant is of particular importance. For the reactions with OH and NH₂, a corresponding deep pre-reactive minimum can be found that contributes to the barrier height and thus slows down the reaction. In general though, abstraction induced by OH radicals is found to be the fastest. The reaction with the H atoms becomes increasingly important at low temperatures, because of the narrow barrier through which tunnelling is efficient. The reaction with NH₂ radicals has both a high and broad barrier and consequently shows significantly smaller low-temperature rate constants.

Key words: astrochemistry – methods: numerical – ISM: molecules.

1 INTRODUCTION

Although the space between the stars seems to be empty and rather hostile for chemical reactions to take place, many molecules have been found in different regions of the interstellar medium (<https://www.astro.uni-koeln.de/cdms>). They range from very simple molecules like CO or H₂O to complex organic molecules (COMs). One such COM is glycine, the simplest amino acid, which is especially interesting with respect to the origin of life and has already been detected in comets (Elsila, Glavin & Dworkin 2009; Altwegg et al. 2016). For the formation of glycine, several possible pathways exist (Sorrell 2001; Garrod 2013). Woon (2002) suggested that the final step towards glycine is the reaction of HOCO and NH₂CH₂, see Fig. 1. This was implemented in an astrochemical model by Garrod (2013) and indeed found to be of importance. This reaction is a recombination of radicals which is expected to be barrier-less and fast. Therefore, the formation of the two radicals is the rate-determining step.

HOCO can be formed via the reaction of CO with OH, studied experimentally by Oba et al. (2011) and Noble et al. (2011) and theoretically by Valero & Kroes (2002), Woon (2002), Nguyen et al.

(2012), Rimola, Sodupe & Ugliengo (2012), Masunov, Wait & Vasu (2016), Tachikawa & Kawabata (2016), and Arasa et al. (2013). The reaction has indeed been seen experimentally to take place at 10 K, indicating a low barrier. However, several calculations show that depending on the local environment this activation energy may change. Here, we take a different approach and investigate the formation of HOCO from formic acid, HCOOH. Formic acid was indeed detected in the pre-stellar core L1544 (Vastel et al. 2014) and in the hot molecular cores G19.61-0.23 and W75N (Remijan et al. 2004) for example. Specifically, we study the radical-induced hydrogen abstraction from the carbon of formic acid by OH (reactions A and B), NH₂ radicals (reaction C), and also H atoms (reaction D) as suggested by Garrod (2013), see also Fig. 2. These types of reactions may lead to the formation of HOCO even when CO is not directly available any more.

In contrast to the reaction of CO with OH, the reactions studied here are hydrogen transfer reactions. This means that due to the low mass of the migrating atom quantum effects, namely atom tunnelling, are more important. Ground state tunnelling is temperature-independent and becomes the dominating part contributing to the rate at the low temperatures in the dense regions of the interstellar medium.

This can be seen by means of an Arrhenius plot of the logarithm of the rate constant k over the inverse temperature T^{-1} . For classical thermal reactions, the Arrhenius plot is linear. But when tunnelling is involved, the Arrhenius plot does not decrease linearly but first bends and then converges to a constant value (see for example Fig. 6). In addition to the dependence on the mass of the moving

* E-mail: a.l.m.lamberts@lic.leidenuniv.nl (TL);

jan.meisner@stanford.edu (JM); kaestner@theochem.uni-stuttgart.de (JK)

† Present address: Department of Chemistry and The PULSE Institute, Stanford University, and SLAC National Accelerator Laboratory, Menlo Park, California 94025, United States.

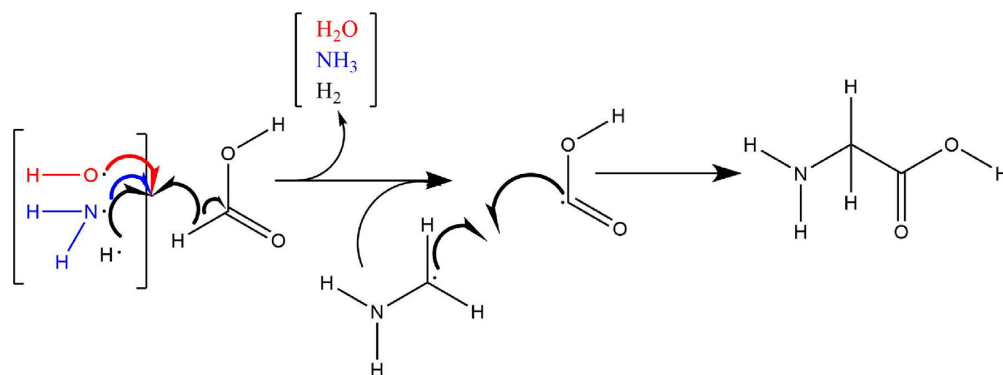


Figure 1. Investigated reactions from formic acid to HOCO and subsequent reaction towards glycine.

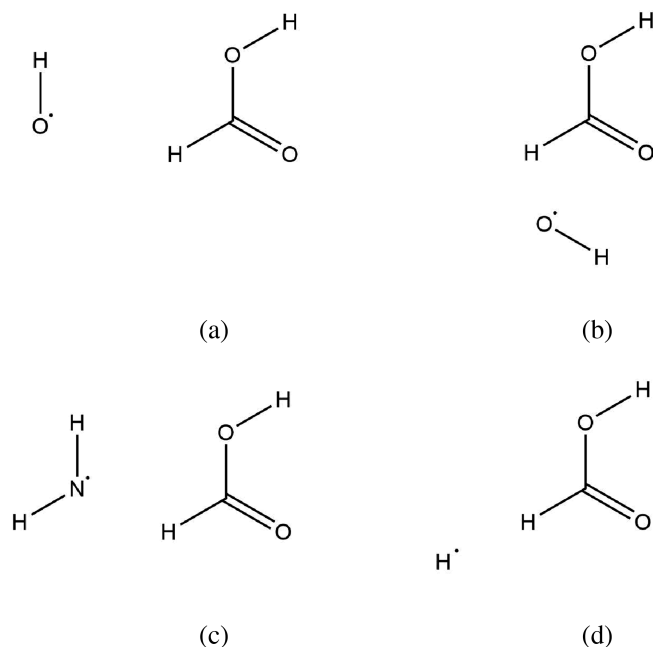


Figure 2. Pre-reactive complexes of the four investigated reactions.

atoms and the barrier height, tunnelling is also influenced by the width of the barrier. The wider a barrier is, the slower the reaction. We use the instanton method to take tunnelling into account.

2 METHODS

Density functional theory (DFT) was chosen as electronic structure method, which offers a good accuracy at reasonable computational effort. The most suitable DFT functional for the reactions was determined through a benchmark of the energies for reaction A (see Fig. 2), whose geometries were optimized with the M06-2X functional (Zhao & Truhlar 2008) and the def2-SVP basis set (Weigend & Ahlrichs 2005). As a reference, CCSD(T)-F12a/cc-pVTZ-F12 single-point energies (Knowles, Hampel & Werner 1993, 2000; Deegan & Knowles 1994; Adler, Knizia & Werner 2007; Peterson, Adler & Werner 2008a; Peterson, Adler & Werner 2008b; Adler, Knizia & Werner 2009; Knizia, Adler & Werner 2009) were calculated for the same geometries with Molpro (Werner et al. 2012) version 2012. Single-point DFT calculations were performed with Turbomole (Ahlrichs et al. 1989) version 7.0.1 and NWChem

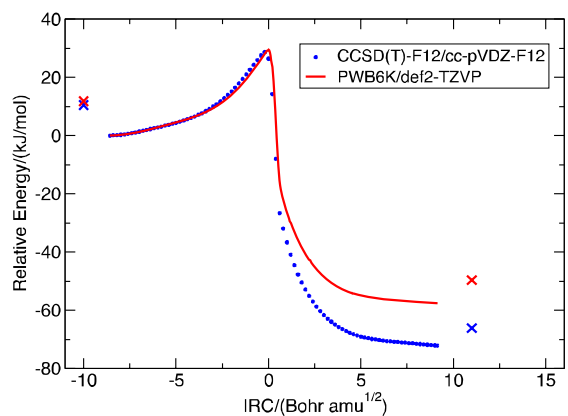


Figure 3. IRC for reaction A with CCSD(T)-F12/cc-pVDZ-F12 single-point energies on every fifth geometry of the PWB6K IRC. Energies of separated reactants and products are denoted with an \times .

(Valiev et al. 2010) version 6.6. All energies for this benchmark were calculated at the same geometries, optimized at the M06-2X/def2-SVP level. The detailed results of the benchmark can be found in Table B5. The combination PWB6K/def2-TZVP (Weigend & Ahlrichs 2005; Zhao & Truhlar 2006), run in NWChem, showed the smallest errors of only 1.08 kJ/mol for the interaction energy of the pre-reactive complex (PRC) and 0.33 kJ/mol for the activation energy of the transition structure, both of which are important for rate constant calculations. In order to confirm this choice of functional, a full intrinsic reaction coordinate (IRC) search with a step-size of 0.04 Bohr $\sqrt{\text{amu}}$ of reaction A was calculated on PWB6K/def2-TZVP level. Single-point CCSD(T)-F12/cc-pVDZ-F12 energies were calculated at every fifth image of the IRC as depicted in Fig. 3. The agreement is very good for reactant and barrier, only towards the product, the energies differ. However, for the following rate constant calculations, mainly the reactant state and the barrier are of interest.

All rate constants reported in this work correspond to reactions on surfaces. Unimolecular rate constants are relevant for the Langmuir-Hinshelwood mechanism (Meisner, Lamberts & Kästner 2017a). To model the influence of the surface, the rotational partition function in the unimolecular case is assumed to be constant during the reaction. Such an implicit surface model (Meisner et al. 2017a) covers the effect of the ice surface, where the rotation on the surface is suppressed. This approximation can be expected to be valid as long as

the reactants are merely physisorbed and the barrier is only weakly affected. This is likely fulfilled for HCOOH on (dirty) CO ice.

We use the instanton method to obtain uni- and bimolecular rate constants including tunnelling (Langer 1967; Miller 1975; Callan & Coleman 1977; Coleman 1977; Kästner 2014). It uses the most likely tunnelling path (the so-called instanton) and a quadratic approximation of its surrounding in contrast to harmonic transition state theory which uses the classical transition state for rate constant calculations. We use canonical instanton theory below the crossover temperature T_c (equation (1), Gillan 1987). Above T_c , the most likely path is the classical reaction path and the instanton path collapses to the transition state. T_c can thus be seen as an indication of the temperature below which tunnelling dominates

$$T_c = \frac{\hbar\Omega}{2\pi k_B}. \quad (1)$$

Here k_B is the Boltzmann constant, \hbar the reduced Planck's constant, and Ω the absolute value of the imaginary frequency of the transition state.

All rate constant calculations were done with DL-Find (Kästner et al. 2009) in Chemshell (Sherwood et al. 2003; Metz et al. 2014). At first, the transition state structure was optimized with the dimer method (Henkelman & Jonsson 1999; Olsen et al. 2004; Heyden, Bell & Keil 2005; Kästner & Sherwood 2008). Pre-reactive complexes and product complexes were optimized from the endpoints of an IRC search, which itself was started at the transition state structure (Hratchian & Schlegel 2004; Meisner et al. 2017b). The, respective, Hessian as well as unimolecular rate constants without tunnelling and with tunnelling approximated by an Eckart barrier (Eckart 1930) were calculated. The former are rate constants in which vibrations are treated by quantum mechanical harmonic oscillators, i.e., zero-point vibrational energy (ZPE) is taken into account. They will be referred to as classical rate constants in the following. In the Eckart model, tunnelling is approximated by the transmission through an Eckart barrier with the same height and crossover temperature as the corresponding reaction (for details see McConnell & Kästner 2017). The first instanton path was optimized from an initial guess along the unstable mode around the transition state. Instanton paths at lower temperatures were optimized from those at higher temperatures. The initial number of images was 40 and was increased if convergence problems occurred (see Tables B1–B4). The temperature interval was also decreased at lower temperatures, to ensure convergence. For reaction D, convergence of the instanton optimization was achieved only down to 70 K, for reaction C to 40 K and for reactions A and B down to 20 K.

3 RESULTS

We investigated the hydrogen abstraction from HCOOH by OH radicals, NH_2 radicals, and H atoms. Only H abstraction from the carbon is investigated, because only this reaction pathway leads to the formation of the glycine precursor HOCO. For the OH radical, two different reaction pathways as found by Anglada (2004) were used. In one of them, the OH radical is near the acidic group of formic acid (reaction A, see Fig. 2), in the other one, the OH radical is near the carbonyl oxygen of formic acid (reaction B). For the reaction with NH_2 or H, only one reaction path was found, each.

The energies along the IRCs for all four reactions are shown in Fig. 4. The energy of the separated reactants and products for each reaction is indicated by the \times -sign in the matching colour. Additionally, a graph with the bimolecular IRCs, relative to these energies can be found in the Appendix (Fig. A1). The energies of

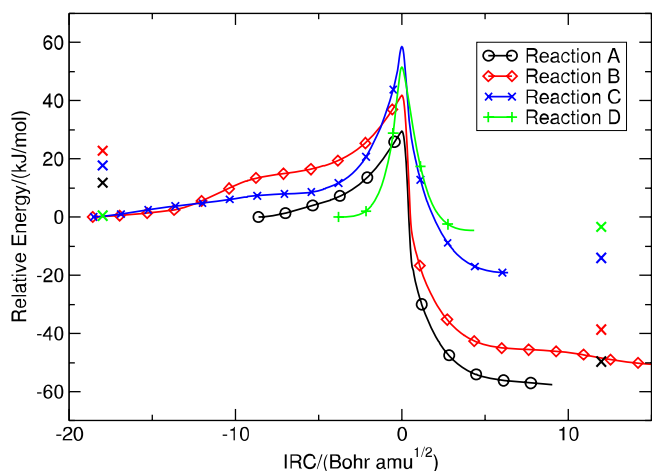


Figure 4. IRCs for the different reactions. The position of the transition state and the energy of the PRC are set to zero Bohr $\sqrt{\text{amu}}$ and kJ/mol, respectively. Note that symbols are drawn only for every 40th point along each path. The \times in the matching colour denotes the energy of the separated reactants and products.

Table 1. Properties of the different reactions. Energies for the PRCs are given relative to separated reactants. Unimolecular activation barriers (ΔE_A) and reaction energies (ΔE_r) are given relative to the PRC. Energies including ZPE correction are given in parentheses. Energies in kJ/mol and crossover temperatures (T_c) in K.

Reaction	PRC	ΔE_A	ΔE_r	T_c
A	-11.8 (-7.9)	29.5 (17.9)	-57.9 (-59.2)	315
B	-22.9 (-16.3)	41.8 (27.0)	-86.2 (-110.4)	324
C	-17.8 (-11.7)	58.7 (50.1)	-19.0 (-16.5)	442
D	-0.4 (0.2)	51.4 (42.9)	-4.7 (-11.1)	379

the PRC with respect to the separated reactants, unimolecular barriers, and reaction energies as well as the crossover temperature are given in Table 1. For the bimolecular values see Table A1. In the unimolecular case, reaction A has the lowest barrier. Reaction B has an intermediate barrier height. Note that the IRC of reaction B is cut off at the product side (see Fig. 4), because a rearrangement takes place after the hydrogen migration. This rearrangement is of no interest for the calculation of the rate constants and will be ignored further on. The reactions C and D have higher barriers. The difference in barrier height for reactions A and B stems from the different PRCs. For reaction A, the energy of the PRC (-11.8 kJ/mol) is not as low as the energy of the PRC of reaction B (-22.9 kJ/mol). This difference in PRC stabilisation of 11.1 kJ/mol is mainly responsible for the difference in unimolecular barrier heights of 12.3 kJ/mol. In the bimolecular case, this is not the case and reactions A and B have similar barrier heights and thus rate constants (see Appendix A).

The IRC is calculated on the bare potential energy surface (PES) without zero-point energy (ZPE). For the important points, the harmonic ZPE correction was calculated (see Table 1). The inclusion of the ZPE changes the energetic properties of the reactions. The energetic stabilization of the PRCs with respect to separated reactants is weaker when ZPE is included. This can be easily explained by the additional vibrational modes that are available in the PRC, as a result of the weakly bonded complex. Similarly, the unimolecular activation energies are lower when ZPE is taken into account, because the unstable mode of the transition state is related to the reaction pathway instead of a vibration. As such it does not contribute

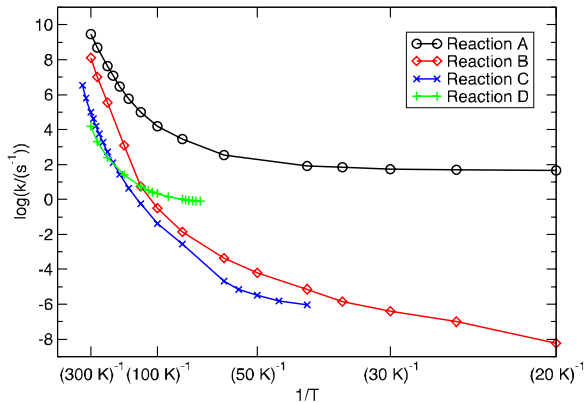


Figure 5. Arrhenius plot of the unimolecular rate constants for the different reactions with the instanton method.

to the ZPE. Furthermore, the ZPE differs for different reactions and should thus always be taken into account.

At high temperatures, the rate constants follow the reverse order of the activation energies, as expected by classical rate theory, see Fig. 5. Reaction A with the lowest activation energy has the highest rate constants, followed by reaction B. At lower temperatures, this changes, however. Here, the classical reaction path over the barrier is no longer applicable, because the thermal energy is not enough to overcome the barrier. Instead, tunnelling through the barrier becomes the main reaction pathway. The mass of the migrating particle is important for tunnelling, but as in all four reactions studied here when a hydrogen atom transfer takes place, the effect of the mass on the rates should be similar. Alongside the height of the barrier, also the width of the barrier is important for tunnelling. This changes the sequence of the rate constants at low temperatures. Reaction A is still the fastest reaction. The barrier is narrow and the rate constant gets nearly temperature-independent below 50 K at a value of about 50 s^{-1} , see Fig. 5. Reactions B and C have broad barriers. Thus, their rate constants still decrease below 50 K because of the increasing width at low impact energies. Especially for Reaction B, one can note that tunnelling has only a small influence down to about 100 K. Fig. 6 clearly shows that the classical rate constant is similar to the instanton rate constant until about 100 K, e.g., at 200 K the instanton rate constant is only a factor of 4 larger than the classical rate constant. This is caused by the hump in the potential energy

prior to the barrier, visible in Fig. 4. Reaction D has the narrowest barrier and, thus, a strong tunnelling contribution. Below 100 K, its rate constant surpasses that of reaction B, despite its higher barrier. At 70 K, the rate constant levels off at a value of about 1 s^{-1} .

4 ASTROPHYSICAL IMPLICATIONS

In astrochemical models, rate constants for the herein presented and other reactions are already used, e.g., by Garrod (2013), with simpler approximations to include tunnelling, like the rectangular barrier (Tielens & Hagen 1982) or the Eckart approximation (Eckart 1930, Taquet et al. (2013)). In Fig. 6, the comparison of the rate constants for different methods is shown. It is clearly visible that neglecting tunnelling (green curve) leads to both qualitatively and quantitatively wrong results in the important temperature range below 100 K. For the calculation of the rate constants with the rectangular barrier, we followed the approach of Hasegawa, Herbst & Leung (1992). The rate constant is calculated as

$$k_{\text{rect}} = v_0 e^{-\frac{2a}{\hbar} \sqrt{2m\Delta E_A}}. \quad (2)$$

Here, v_0 is the attempt frequency which was assumed to be 10^{12} s^{-1} . The barrier width a is set to 1 \AA as is commonly done in models. Because all reactions are hydrogen transfer reactions, the effective mass m was set equal to the mass of hydrogen. The reaction barriers, ΔE_A , were taken from our calculations for the unimolecular cases including ZPE corrections. Thus, the difference in the rate constants only depends on the barrier height and neglects the differences in barrier width that are crucial for tunnelling. When the barrier width a would not be set to 1 \AA but fitted to the investigated reaction, this could be improved. Also, the rate obtained with this method is independent of temperature, leading to bad descriptions of reaction B and C where the rate constant still decreases even at low temperatures.

The Eckart approximation includes tunnelling in rate constants by multiplying the classical rate constant with a tunnelling correction factor κ . This correction factor is calculated by approximating the barrier as an Eckart barrier. This approximation is good if the tunnelling path is similar to the classical reaction path on which the Eckart approximation is based. At low temperatures, the tunnelling path can, however, differ a lot from the classical reaction path by corner cutting (Marcus & Coltrin 1977; Meisner et al. 2017b). In our reactions, the Eckart approximation overestimates the rate constants at low temperatures. In general, both the rectangular barrier

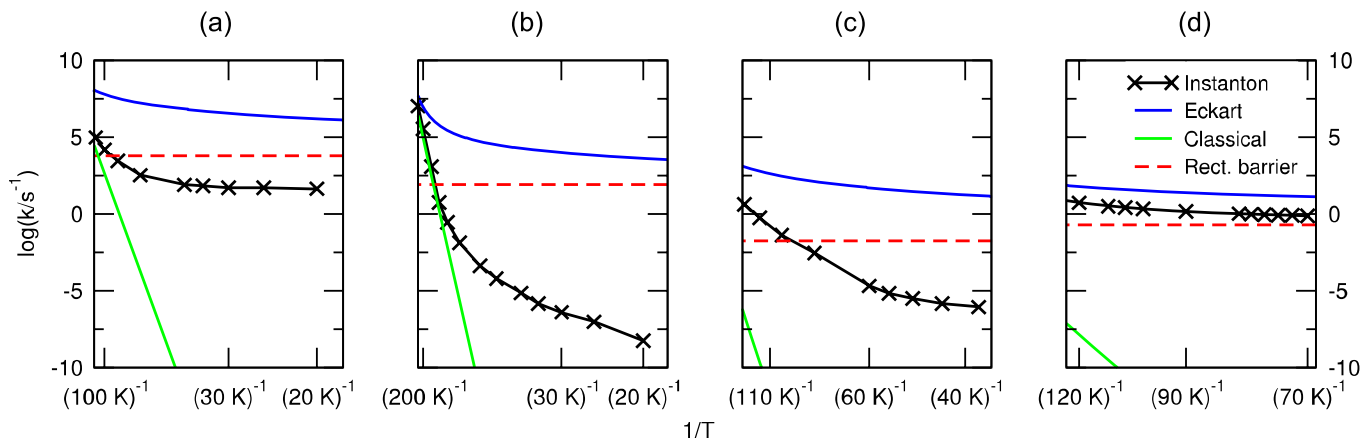


Figure 6. Arrhenius plots of the rate constants for the reactions in the astrochemically important temperature range, with different methods. Instanton (black), Eckart (blue), rectangular barrier (red), and classical including ZPE correction (green).

and Eckart approximations cannot be trusted throughout the full temperature range for all reactions.

More specifically, when we compare the low-temperature values calculated here to those implemented by, e.g., Garrod (2013) (table 3, with $m = 1$ amu), the values we obtained with instanton theory are much smaller for reactions A, B, and C by at least 4 orders of magnitude, but the value for the abstraction of H by an H atom (reaction D) is two orders of magnitude higher. In other words, it would depend heavily on the local radical abundance whether or not these reactions contribute to HOCO formation.

As mentioned before, an alternative way to form HOCO is through the direct reaction of CO and OH. Unfortunately, the various theoretical works available show that the existence or absence of an activation barrier is strongly dependent on the local environment, e.g., gas-phase calculations versus the explicit inclusion of a H₂O or CO₂ molecule or H₂O cluster (Masunov et al. 2016; Tachikawa & Kawabata 2016). The barriers involved are low, however, i.e. <750 K. A direct comparison of the reaction paths leading to HOCO via HCOOH or CO + OH is not possible using rate constants alone. What should be compared are the final rates, which include information on the concentration. Implementation of all rate constants in an astrochemical model will be able to show which reaction routes dominate in which interstellar regions for the formation of HOCO.

As a final note, we want to comment on the fact that in this work the reactions are studied without the inclusion of explicit surface molecules. The influence of surface molecules can, but does not always, have an influence on the activation energy of a reaction, compare for instance Meisner et al. (2017a) and Lamberts & Kästner (2017). The latter study indicates that even for a reaction where the influence on the activation energy is large, this results at most in a difference in the rate constant of about two orders of magnitude, which means that our comparison to currently implemented values is still valid. A surface can, however, have a pronounced effect on the orientation of the reactants on the surface. This may prevent or enhance particular reaction routes.

5 CONCLUSIONS

We calculated unimolecular rate constants for the hydrogen abstraction from formic acid to form HOCO by different radicals, OH, NH₂, and H, down to low temperatures with the instanton method. For reactions A (with OH) and D (with H), the Arrhenius plot shows a nearly constant course at low temperatures (below 90 K). Reactions B (with OH) and C (with NH₂) do not show this behaviour, at low temperatures the course of the Arrhenius plot is still decreasing. Thus, these reaction pathways may be less important at low temperatures. The overall highest rate constants were found for reaction A, which also had the lowest barrier. Reaction D has a high but narrow barrier, which leads to low rate constants at high temperatures but comparably high rate constants at low temperatures. The simpler Eckart approximation cannot be used for low temperatures, because its rate constants show large deviations from the instanton results. The rate constants calculated here can be implemented in astrochemical models.

ACKNOWLEDGEMENTS

This work was financially supported by the German Research Foundation (DFG) within the Cluster of Excellence in Simulation Technology (EXC 310/2) at the University of Stuttgart and the European Union's Horizon 2020 Research and Innovation Programme (Grant Agreement 646717, TUNNELCHEM). The authors

acknowledge support by the state of Baden-Württemberg through bwHPC and the German Research Foundation (DFG) through grant no INST 40/467-1 FUGG. Thanja Lamberts acknowledges the Alexander von Humboldt Foundation and the Netherlands Organisation for Scientific Research (NWO) via a Veni fellowship (722.017.008) for generous support. This project was supported by an STSM travel grant within the COST Action CM1401 'Our Astro-Chemical History'.

REFERENCES

- Adler T. B., Knizia G., Werner H.-J., 2007, *J. Chem. Phys.*, 127, 221106
Adler T. B., Knizia G., Werner H.-J., 2009, *J. Chem. Phys.*, 130, 054104
Ahlrichs R., Baer M., Haeser M., Horn H., Koelmel C., 1989, *Chem. Phys. Lett.*, 162, 165
Altwegg K. et al., 2016, *Sci. Adv.*, 2
Anglada J. M., 2004, *J. Am. Chem. Soc.*, 126, 9809
Arasa C., van Hemert M. C., van Dishoeck E. F., Kroes G. J., 2013, *J. Phys. Chem. A*, 117, 7064
Callan C. G., Jr, Coleman S., 1977, *Phys. Rev. D*, 16, 1762
Coleman S., 1977, *Phys. Rev. D*, 15, 2929
Deegan M. J. O., Knowles P. J., 1994, *Chem. Phys. Lett.*, 227, 321
Eckart C., 1930, *Phys. Rev.*, 35, 1303
Elsila J. E., Glavin D. P., Dworkin J. P., 2009, *Meteorit. Planet. Sci.*, 44, 1323
Garrod R. T., 2013, *ApJ*, 765, 60
Gillan M. J., 1987, *J. Phys. C*, 20, 3621
Hasegawa T. I., Herbst E., Leung C. M., 1992, *ApJS*, 82, 167
Henkelman G., Jonsson H. J., 1999, *J. Chem. Phys.*, 111, 7010
Heyden A., Bell A. T., Keil F. J., 2005, *J. Chem. Phys.*, 123, 224101
Hratchian H. P., Schlegel H. B., 2004, *J. Chem. Phys.*, 120, 9918
Kästner J., 2014, *WIREs Comput. Mol. Sci.*, 4, 158
Kästner J., Sherwood P., 2008, *J. Chem. Phys.*, 128, 014106
Kästner J., Carr J. M., Keal T. W., Thiel W., Wander A., Sherwood P., 2009, *J. Phys. Chem. A*, 113, 11856
Knizia G., Adler T. B., Werner H.-J., 2009, *J. Chem. Phys.*, 130, 054104
Knowles P. J., Hampel C., Werner H.-J., 1993, *J. Chem. Phys.*, 99, 5219
Knowles P. J., Hampel C., Werner H.-J., 2000, *J. Chem. Phys.*, 112, 3106
Lamberts T., Kästner J., 2017, *ApJ*, 846, 43
Langer J. S., 1967, *Ann. Phys. (N.Y.)*, 41, 108
Marcus R. A., Coltrin M. E., 1977, *J. Chem. Phys.*, 67, 2609
Masunov A. E., Wait E., Vasu S. S., 2016, *J. Phys. Chem. A*, 120, 6023
McConnell S. R., Kästner J., 2017, *J. Comput. Chem.*, 38, 2570
Meisner J., Lamberts T., Kästner J., 2017a, *ACS Earth Space Chem.*, 1, 399
Meisner J., Markmeyer M. N., Bohner M. U., Kästner J., 2017b, *Phys. Chem. Chem. Phys.*, 19, 23085
Metz S., Kästner J., Sokol A. A., Keal T. W., Sherwood P., 2014, *WIREs Comput. Mol. Sci.*, 4, 101
Miller W. H., 1975, *J. Chem. Phys.*, 62, 1899
Nguyen T. L., Xue B. C., Jr, R. E. W., Berker J. R., Stanton J. F., 2012, *J. Phys. Chem. Lett.*, 3, 1549
Noble J. A., Dulieu F., Congiu E., Fraser H. J., 2011, *ApJ*, 735, 121
Oba Y., Watanabe N., Kouchi A., Hama T., Pirronello V., 2011, in Cernicharo J., Bachiller R., eds, *IAU Symposium Vol. 280, The Molecular Universe*. Cambridge University Press, Cambridge, UK, p. 278
Olsen R. A., Kroes G. J., Henkelman G., Arnaldsson A., Jonsson H. J., 2004, *J. Chem. Phys.*, 121, 9776
Peterson K., Adler T., Werner H.-J., 2008a, *J. Chem. Phys.*, 128, 084102
Peterson K. A., Adler T. B., Werner H.-J., 2008b, *J. Chem. Phys.*, 128, 084102
Remijan A., Shiao Y.-S., Friedel D. N., Meier D. S., Snyder L. E., 2004, *ApJ*, 617, 384
Rimola A., Sodupe M., Ugliengo P., 2012, *ApJ*, 754, 24
Sherwood P. et al., 2003, *J. Mol. Struct. (Theochem.)*, 632, 1
Sorrell W. H., 2001, *ApJ*, 555, L129
Tachikawa H., Kawabata H., 2016, *J. Phys. Chem. A*, 120, 6596
Taquet V., Peters P., Kahane C., Ceccarelli C., Lopez-Sepulcre A., Toubin C., Duflot D., Wiesenfeld L., 2013, *A&A*, 550, A127

Tielens A. G. G. M., Hagen W., 1982, *A&A*, 114, 245
 Valero R., Kroes G.-J., 2002, *J. Chem. Phys.*, 117, 8736
 Valiev M. et al., 2010, *Comput. Phys. Commun.*, 181, 1477
 Vastel C., Ceccarelli C., Lefloch B., Bachiller R., 2014, *ApJ*, 795, L2
 Weigend F., Ahlrichs R., 2005, *Phys. Chem. Chem. Phys.*, 7, 3297
 Werner H.-J., Knowles P. J., Knizia G., Manby F. R., Schütz M., 2012, *WIREs Comput. Mol. Sci.*, 2, 242
 Woon D. E., 2002, *ApJ*, 571, L177
 Zhao Y., Truhlar D. G., 2006, *J. Chem. Phys.*, 124, 224105
 Zhao Y., Truhlar D. G., 2008, *Theor. Chem. Acc.*, 120, 215

APPENDIX A: THE BIMOLECULAR CASE

The bimolecular rate constants derived here describe the reaction in the gas phase, where separated molecules meet and react. Here, the PRC does not play a role, the rates are calculated with respect to the separated reactants. Therefore, regions below the energy of the separated reactions are not considered in the IRCs. The instanton obtained for the unimolecular case is used, but bimolecular instanton rate constants are only available down to 120 K, where the tunnelling energy of the instanton path is at least as high as the energy of the separated reactants.

The inclusion of ZPE for the activation energies lowers the barrier, similar to the unimolecular case. This is because the C–H vibration in the separated reactant formic acid, that has a large contribution to the ZPE, is no longer active in the TS because it follows the transition mode. The new vibrational modes that are associated with the interaction of the two former separated reactants have low contributions to the ZPE and cannot compensate its loss, leading to a net reduction of the activation energy. The barriers of reactions A and B are very similar in height (see Table A1) and shape (see Fig. A1) unlike the unimolecular case where the different PRCs caused a large difference. Therefore, also the rate constants are similar (see Fig. A2). These exceed the values for reaction C and D, due to their lower barrier height. Because bimolecular rate constants were only available down to 120 K, tunnelling does not yet play such an important role.

Table A1. Energies for bimolecular barrier (ΔE_A) and reaction energy (ΔE_r) relative to separated reactants in kJ/mol. Energies including ZPE correction are given in parentheses.

Reaction	ΔE_A	ΔE_r
A	17.7 (10.0)	−61.5 (−62.1)
B	18.9 (10.7)	−61.5 (−62.1)
C	40.9 (38.4)	−31.7 (−25.9)
D	51.0 (43.1)	−3.8 (−12.3)

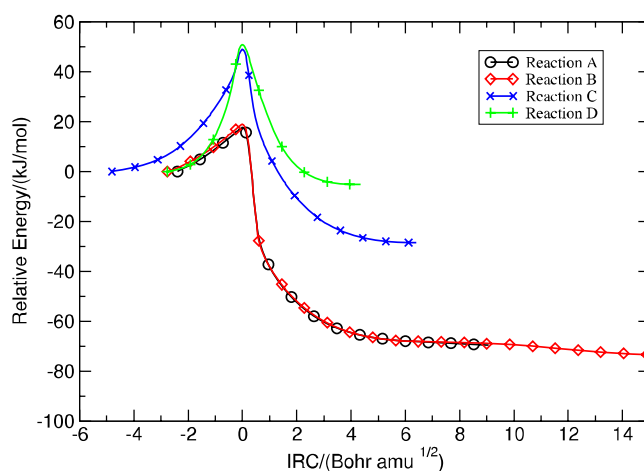


Figure A1. Bimolecular IRCs for the different reactions. The position of the transition state and the energy of the separated reactants are set to zero Bohr $\sqrt{\text{amu}}$ and kJ/mol, respectively. Note that symbols are drawn only for every 20th point along each path. Energies below the energy of the separated reactants on the reactant side of the barrier are cut off to show only the part of the barrier that is significant for bimolecular rate constants.

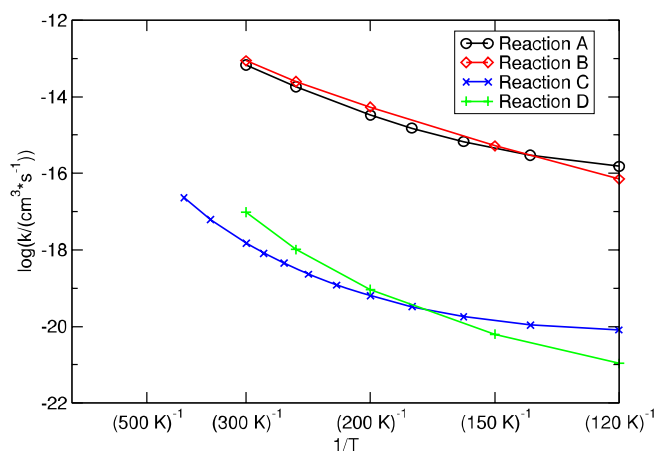


Figure A2. Arrhenius plot of the bimolecular rate constants for the different reactions with the instanton method.

APPENDIX B: RATE CONSTANTS AND BENCHMARK

Table B1. Rate constants with the instanton method for reaction A.

Temperature T/K	Number of images	Unimolecular $\log(k/s^{-1})$	Bimolecular $\log(k/(cm^3 \cdot s^{-1}))$
300	40	9.48	-13.17
250	40	8.71	-13.74
200	40	7.63	-14.48
180	40	7.10	-14.82
160	40	6.48	-15.17
140	40	5.77	-15.53
120	40	4.99	-15.82
100	40	4.19	
80	78	3.45	
60	154	2.53	
40	154	1.90	
35	154	1.83	
30	154	1.72	
25	154	1.71	
20	306	1.65	

Table B2. Rate constants with the instanton method for reaction B.

Temperature T/K	Number of images	Unimolecular $\log(k/s^{-1})$	Bimolecular $\log(k/(cm^3 \cdot s^{-1}))$
300	40	8.11	-13.06
250	40	7.03	-13.61
200	40	5.54	-14.27
150	78	3.08	-15.28
120	78	0.76	-16.15
100	78	-0.52	
80	154	-1.87	
60	154	-3.36	
50	154	-4.21	
40	154	-5.14	
35	154	-5.84	
30	154	-6.39	
25	154	-7.01	
20	306	-8.24	

Table B3. Rate constants with the instanton method for reaction C.

Temperature T/K	Number of images	Unimolecular $\log(k/s^{-1})$	Bimolecular $\log(k/(cm^3 \cdot s^{-1}))$
400	40	6.53	-16.64
350	40	5.82	-17.21
300	40	4.99	-17.82
280	40	4.61	-18.09
260	40	4.21	-18.35
240	40	3.75	-18.64
220	40	3.26	-18.92
200	78	2.73	-19.20
180	78	2.11	-19.48
160	78	1.42	-19.75
140	78	0.64	-19.96
120	78	-0.25	-20.09
100	154	-1.38	
80	154	-2.55	
60	154	-4.68	
55	306	-5.15	
50	306	-5.50	
45	306	-5.81	
40	306	-6.05	

Table B4. Rate constants with the instanton method for reaction D.

Temperature T/K	Number of images	Unimolecular $\log(k/s^{-1})$	Bimolecular $\log(k/(cm^3 \cdot s^{-1}))$
300	40	4.20	-17.02
250	40	3.33	-17.99
200	40	2.41	-19.04
150	40	1.39	-20.20
120	78	0.74	-20.97
110	154	0.52	
105	154	0.42	
100	154	0.33	
90	154	0.17	
80	154	0.03	
78	306	-0.02	
76	306	-0.04	
74	306	-0.07	
72	306	-0.09	
70	306	-0.11	

Table B5. Energies of the benchmarked methods relative to the separated reactants in kJ/mol.

Method	PRC	Transition state	Unimolecular barrier	Product complex	Separated products
Molpro					
CCSDT-F12/VDZ-F12	-9.6	16.9	26.5	-77.3	-67.7
CCSDT-F12/VTZ-F12	-9.9	16.5	26.4	-78.0	-68.1
Turbomole					
Basis: DEF2-SVP					
B3-LYP	-15.3	-13.6	1.7	-63.5	-48.2
PBE	-19.1	-51.2	-32.2	-80.4	-61.4
PBE0	-15.2	-11.1	4.1	-63.6	-48.3
BP86	-13.3	-44.6	-31.3	-78.9	-65.6
BHLYP	-14.7	21.8	36.5	-42.0	-27.3
TPSS	-15.1	-29.8	-14.7	-59.9	-44.7
TPSSH	-14.8	-15.8	-1.0	-55.2	-40.4
M06	-19.4	-10.0	9.4	-67.8	-48.3
M06-2X	-21.4	6.3	27.7	-64.0	-42.6
Basis: DEF2-TZVP					
B3-LYP	-8.2	-5.3	2.9	-70.1	-61.8
PBE	-5.5	-44.1	-38.5	-88.1	-82.5
PBE0	-9.0	-4.8	4.1	-70.5	-61.5
BP86	-0.8	-38.0	-37.2	-86.4	-85.5
BHLYP	-8.3	29.2	37.5	-47.8	-39.5
TPSS	-2.6	-23.8	-21.2	-68.1	-65.5
TPSSH	-7.7	-9.9	-2.2	-63.0	-55.3
M06	-12.9	-1.2	11.7	-70.3	-57.4
M06-2X	-14.8	13.3	28.1	-70.6	-55.9
NWChem					
Basis: DEF2-SVP					
M06-2X	-21.3	5.9	27.2	-63.0	-41.7
M06-HF	-22.7	28.7	51.4	-53.6	-30.9
M06-L	-17.3	-22.8	-5.5	-62.1	-44.8
M06	-19.3	-10.7	8.6	-68.0	-48.7
M08-HX	-20.3	7.0	27.3	-66.1	-45.8
M08-SO	-19.1	6.3	25.4	-60.6	-41.4
M11-L	-11.4	0.3	11.7	-80.9	-69.5
M11	-18.3	8.2	26.5	-72.2	-53.9
Basis: DEF2-TZVP					
M06-2X	-14.8	13.0	27.8	-70.2	-55.4
M06-HF	-14.5	33.7	48.2	-68.6	-54.0
M06-L	-13.7	-16.7	-3.0	-65.6	-51.8
M06	-13.1	-1.5	11.7	-72.5	-59.9
M08-SO	-11.9	14.4	26.2	-67.6	-55.8
M11-L	-6.0	9.0	15.1	-75.4	-69.4
M11	-11.2	12.9	24.1	-81.4	-70.2
Basis: DEF2-SVPD					
M06-2X	-16.4	9.7	26.1	-74.9	-58.5
M08-HX	-14.5	10.7	25.3	-80.2	-65.7
M08-SO	-13.7	10.3	23.9	-73.4	-59.7
M11	-12.2	12.3	24.5	-86.2	-74.0
Basis: DEF2-TZVPD					
M06-2X	-13.4	13.6	27.0	-74.0	-60.6
M08-HX	-10.3	15.2	25.5	-76.2	-65.9
M08-SO	-10.4	14.8	25.3	-71.3	-60.8
M11	-9.5	13.6	23.1	-85.0	-75.5
Basis: DEF2-SVP					
MPW1B95	-15.6	-7.4	8.2	-66.6	-51.0
MPWB1K	-14.8	8.2	23.0	-58.2	-43.4
PW6B95	-17.0	-9.2	7.8	-65.3	-48.3
PWB6K	-17.1	9.6	26.7	-55.3	-38.2
Basis: DEF2-TZVP					
MPW1B95	-9.1	0.1	9.2	-73.1	-64.0
MPWB1K	-8.6	15.3	23.8	-64.3	-55.8
PW6B95	-10.4	-1.3	9.1	-71.9	-61.4
PWB6K	-10.9	16.8	27.8	-61.5	-50.5